Research Article Vol. 30, No. 4 / 14 Feb 2022 / Optics Express 6397
Optics EXPRESS

Optical performance monitoring using SOI-based spectral analysis

ZHUILI HUANG,[1] YE TIAN,[2] YUFEI LIU,[1,4] HUAIJIAN LUO,[3,5] XIAOJING LONG,[1] AND CHANGYUAN YU[3]

[1]*Key Laboratory of Optoelectronic Technology & Systems (Ministry of Education), College of Optoelectronic Engineering, Chongqing University, Chongqing, 400044, China*
[2]*Department of Electrical Engineering and Computer Science, Ningbo University, Ningbo 315211, China*
[3]*Photonics Research Centre, Department of Electronics and Information Engineering, The Hong Kong Polytechnic University, Hong Kong, China*
[4]*yufei.liu@cqu.edu.cn*
[5]*huaijian.luo@connect.polyu.hk*

Abstract: A novel optical performance monitoring (OPM) method based on Fourier transform spectrum analysis (FTSA) is designed for optical signal-to-noise ratio (OSNR) monitoring, modulation format and baud rate recognition in the presence of fiber nonlinearities. The interference intensities, which reflect spectral features of signals, are obtained by exploiting the FTSA consisting of two-stage Mach-Zehnder interferometer (MZI) arrays. Then, the mapping between the OPM parameters and modulated interference intensity (MII) is characterized using neural networks without prior knowledge of the configuration of the communication network. Results show that optical performance parameters are monitored simultaneously. Meanwhile, the accuracy of modulation format and baud rate recognition is 94.8% and most (over 86%) OSNR monitoring errors are less than ±1 dB under complex transmission conditions in presence of frequency offset and delay jitter. Besides, the FTSA can be fabricated on a silicon on insulator (SOI) platform with a large fabrication tolerance, and it has broad working bandwidth to support the full optical communication band. Therefore, the proposed OPM method is capable of integration and miniaturization, which can be ubiquitously applied in network intermediate nodes to support the construction of smart optical networks.

1. Introduction

With the continuous development of high-bandwidth network services, such as cloud, virtual reality (VR), fifth-generation mobile communications (5G), and the Internet of Things (IoT), optical network capacity demand is ever-increasing [1,2]. To improve bandwidth and spectral efficiency, the dense wavelength division multiplexing (DWDM) technique, advanced modulation format, polarization multiplexing technology, and elastic optical networks have been widely adopted in optical networks [3]. In elastic optical networks, channel configurations including modulation format, symbol rate, and launch power can be fully optimized to maximize the capacity of the physical layer infrastructure [4]. Therefore, optical performance monitoring (OPM) has been a key supporting technology to guarantee adaptively monitoring and management for dynamic optical networks, which ensure optimum resource utilization and reduce operating costs.

The optical signal-to-noise ratio (OSNR) is one of the most important OPM parameters because it is directly related to bit error rate (BER) which reflects the quality of the optical network [5]. Therefore, many OSNR monitoring methods have been proposed, such as polarization nulling [6], Stokes parameter [7], normalized autocorrelation function [8], reference optical spectrum [9], and so on. Besides, the recognition of modulation format and baud rate is indispensable. On the one hand, it enables the flexible networks to adjust modulation formats and baud rates

#451269 https://doi.org/10.1364/OE.451269
Journal © 2022 Received 16 Dec 2021; revised 22 Jan 2022; accepted 3 Feb 2022; published 11 Feb 2022

Optics EXPRESS

dynamically based on transmission conditions [10]. On the other hand, the digital signal processing (DSP) algorithm also needs to match the modulation format and baud rate of the signal [11]. Likelihood-based (LB) and features-based (FB) methods have been proposed, which require a prior knowledge of channel parameters and/or a comprehensible mathematical model describing the channel under consideration [12].

In the last decade, machine learning (ML) has triggered widespread interest in optical network research, such as nonlinearity compensation [13], nonlinear equalizer design [14–16], optical channel modeling [17], and OPM. The signal features for ML-based OPM include asynchronous amplitude histograms (AAH) [18–20], asynchronous delay-tap sampling portraits (ADTPs) [21,22], eye diagram [23], constellation diagram [24–26], auto-covariance function [27], and tunable optical bandpass filter (OBPF) [28,29], etc. With the increasing interest and activities in ML, there is a wide variety of algorithm models applied in OPM. They include but are not limited to artificial neural networks (ANNs) [30], deep neural networks (DNNs) [20], convolutional neural networks (CNNs) [19,22,24], long short-term memory (LSTM) network [32], principal component analysis (PCA) [33], and Gaussian process regression (GPR) [29,34]. Although many techniques can achieve the target of OPM, some deep learning networks with large hyperparameters are computationally complicated and thus time-consuming. Meanwhile, a large dataset is needed for these types of networks which also impedes the training process. Although the graphics processing unit (GPU) is able to speed up significantly the training for a complex model, it is still not cost-effective for large-scale schemes [25,31]. It is worth noting that the long haul and high-capacity backbone transmission systems require higher launch power, which will trigger fiber nonlinearity. Therefore, optical performance monitoring methods, which can be applied in scenarios with fiber nonlinearity, are highly recommended [35]. In this paper, we focus on OSNR monitoring and recognition of modulation format and baud rate with relatively simple ANNs in presence of fiber nonlinearities.

On a parallel development, silicon on insulator (SOI) platform is attractive for optical performance monitoring owing to its high transparency in telecom wavelength band, and compatibility with well-established complementary metal oxide semiconductor (CMOS) processes. The OPM device capable of integration significantly simplifies assembly processes and drastically reduces the size and cost. Thus, lots of integrated OPM devices have been reported [36–38]. In [36], the scheme based on liquid crystal on silicon is suitable for large-scale OSNR monitoring, but the control of the optical path is complex. In [37], Tanizawa et al. first reported a fully-passive in-band OSNR monitor integrated on an SOI wafer, utilizing the difference of the time variance in the states of polarization (SOP) between signal and noise, and they mainly investigated the OSNR monitoring of single-polarization signals. In our previous work [38], we proposed an OSNR monitoring method based on asymmetrical parallel Mach-Zehnder interferometers, which needs a heater to introduce phase shift to obtain the maximum and minimum power. However, the heater takes extra energy and time.

To address the aforementioned issue, we propose a novel OPM method based on the Fourier transform spectrum analyzer (FTSA) with artificial neural networks in this paper. The FTSA is used to obtain interference intensities, which are related to optical performance parameters. The FTSA works without heaters, which effectively simplifies the OPM procedures and improves efficiency. ANN models achieve the mapping between the modulated interference intensities (MIIs) and multiple OPM parameters without prior knowledge of network configuration, such as transmission distance, the quantity of channels, launch power, etc. The results show that for polarization multiplexing 12.5/25 Gbaud QPSK/16QAM signals, over 86% of OSNR monitoring errors are distributed within ±1 dB with a range from 5 to 30 dB. The accuracy of modulation format and baud rate recognition is 94.8%. Results also show that the proposed method works well as the launch power of each channel changes from 0 to 6 dBm with a fiber link of 320–1600 km, and the delay jitter range varies from −0.5 to +0.5 ps.

Optics EXPRESS

2. Operation principle

2.1. Fourier transform spectrum analyzer

As shown in Fig. 1(a), the proposed FTSA is designed on the SOI platform with a 220 nm-thick silicon layer and a 2 μm-thick buried oxide layer. It is composed of two-stage Mach-Zehnder interferometers (MZIs). The first stage contains a single MZI, and the second stage is an MZI array with different delay values. Each MZI is composed of two 1×2 multimode interferences (MMIs) and ridge waveguides, which are set as 500-nm in width to support fundamental TE mode propagation. The length difference between two ridge waveguides corresponds to the optical path difference (OPD) between the two arms in MZI. The two stages of MZIs are connected by a 1×N power splitter with a uniform splitting ratio. The interference intensities are received by an array of integrated Ge-on-Si photodetectors (PDs) after the MZI array.

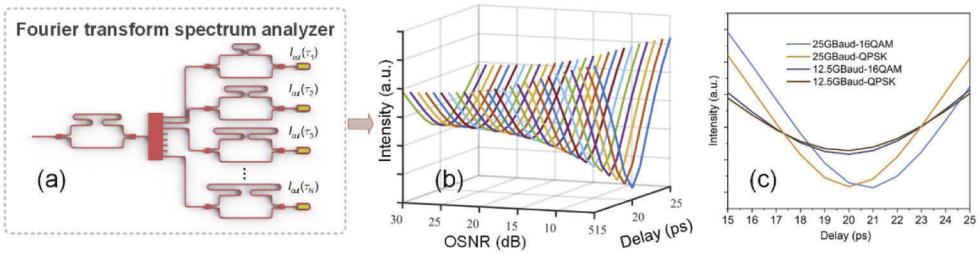

Fig. 1. (a) Schematic configuration of Fourier transform spectrum analyzer. (b) Modulated interference intensities of different OSNR. (c) Modulated interference intensities of 12.5/25 Gbaud QPSK/16QAM signals with the same transmission configuration.

For super-narrow input spectrum $S(v_0)$ with the central wavelength v_0, the output of the MZI in the first stage I_m can be written as

$$I_m = T_1(v, \tau_0) \cdot S(v_0) \tag{1}$$

where T_1 and τ_0 are the transmission function and delay of the MZI in the first stage, respectively. The output intensity of the MZI in the second stage can be expressed as

$$I_{out}(\tau) = \frac{1}{N} T_2(v, \tau) \cdot T_1(v, \tau_0) \cdot S(v_0) \tag{2}$$

where T_2 and τ are the transmission function and the delay of the MZI in the second stage, respectively. N indicates that the signal is separated into N parts by the power splitter for transmission into the second MZI array. The transmission function for MZI can be written as follows

$$T(\tau) = \frac{1}{2} + \sqrt{\alpha(1-\alpha)} \cos(2\pi v \tau) \tag{3}$$

$$\tau = n_{eff} \cdot \Delta L / c \tag{4}$$

where α, n_{eff}, $\triangle L$ are split ratio, effective refractive index, OPD of the MZI, respectively. c is the velocity of light. The extinction ratio is

$$ER = \frac{1 + 2\sqrt{\alpha(1-\alpha)}}{1 - 2\sqrt{\alpha(1-\alpha)}}. \tag{5}$$

In practice, some factors will influence the signal intensity detected by the detector. The ratio of the beam splitter is not perfect as 1:1 ($\alpha = 0.5$) due to the fabrication error. Light will

Optics EXPRESS

experience losses in beam splitters and waveguides of MZI arms, etc. As a result, with the simplification that the above factors are separable, the output intensity should be modified as

$$I_{out}(\tau) = \frac{0.5}{N} H(v)G(v)T_1(v,\tau_0)S(v_0)(1+\cos(2\pi v\tau)) \tag{6}$$

where $H(v)$ and $G(v)$ are transmission functions of beam splitters and optical losses, respectively. We set the coefficient $\frac{0.5}{N}H(v)G(v)T_1(v,\tau_0)$ as $B(v)$, then the relation between input spectrum and output intensity can be simplified as

$$I_{out}(\tau) = B(v)S(v_0)(1+\cos(2\pi v\tau)) \tag{7}$$

where $B(v)S(v_0)$ is the constant intensity portion, and $B(v)S(v_0)\cos(2\pi v\tau)$ is the modulated portion. Taking the modulated portion into consideration only, the output intensity for a broadband input spectrum is

$$I_{out}(\tau) = \int_{-\infty}^{+\infty} B(v)S(v)\cos(2\pi v\tau)dv \tag{8}$$

After applying Fourier transform to the above equation, the input spectrum can be obtained as

$$S(v) = \frac{2}{B(v)}\int_{0}^{+\infty} I_{out}(\tau)\cos(2\pi v\tau)d\tau \tag{9}$$

The output intensity $I_{out}(\tau)$ and the input spectrum $S(v)$ are a Fourier transform pair [39,40]. Therefore, the rough input spectrum can be reconstructed through the output intensities of the MZI array.

According to our previous work [8], the optical performance parameters are related to the shape of the spectrum, thus the optical performance parameters can be extracted through the output intensities. To remove the effect of absolute intensity on the OPM performance, we subtract the mean value of intensity from the detected intensity as a simple preprocessing procedure as follow

$$I^m_{out}(\tau) = I_{out}(\tau) - mean(I_{out}(\tau)) \tag{10}$$

where $I^m_{out}(\tau)$ is defined as modulated interference intensity (MII). As shown in Fig. 1(b), the MII varies with the change of OSNR value because the spectra are distinct for different OSNR. Similarly, intensities distribution varies along with the modulation format and baud rate as well, as shown in Fig. 1(c) where the OSNR, the quantity of channels, launch power, transmission span of signals are set to 20 dB, 3, 1 dBm, 20, separately, i. e., the variables are just modulation format and baud rate. Therefore, the information of OSNR, modulation format, and baud rate can be acquired by analyzing the MII. However, characterizing the mapping between the OPM parameters and the change of MII is believed to be analytically intractable because many variables could influence MII with different degrees. Therefore, we propose to use neural networks (NNs) to automatically extract the OSNR, modulation format, and baud rate. However, it is hard for the method to discriminate the OSNR of the signals in the Nyquist super-channel because the spectrum of signals and the spectrum of ASE noise are both flat. The application of the Nyquist super-channel is left for our future work.

2.2. Artificial neural networks

Generally, there are two kinds of ANN in terms of the type of the output, i.e. the regression and the classification model [41]. In Fig. 2, the recognition of the modulation format and baud rate is a classification problem, which is solved by a two-layer feed-forward network with the *sigmoid* activation function in the hidden layer and the *softmax* activation function in the output layer

Optics EXPRESS

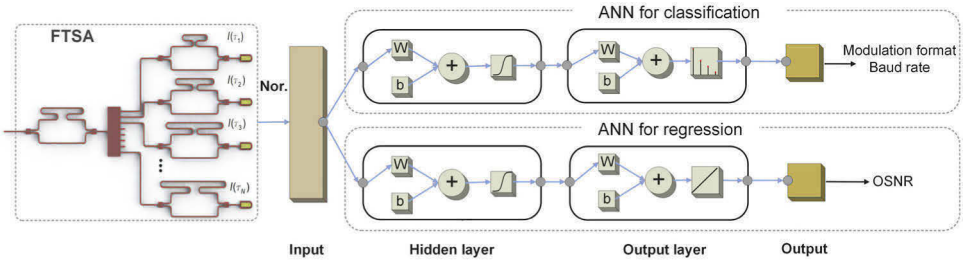

Fig. 2. The block diagram of the proposed ANNs for OPM.

(ANN for classification). The OSNR estimation is a regression problem, which is also solved by a two-layer neural network (ANN for regression). The activation function of the output layer in this model is *linear* instead of *softmax*.

Compared to other neural networks, such as CNN, LSTM, and DNN, a shallow ANN is easier to train but its function is relatively simple and requires more manual preprocessing efforts. Therefore, an appropriate feature needs to be selected to reduce the complexity. Here we select the MIIs as the training features of neural networks because of their simplicity. The hidden layer has tunable numbers of neurons. The output of the *rth* neuron can be expressed as

$$yr = f(\sum_{i} wrixi + br) \tag{11}$$

where *xi* is the *ith* input to the neuron, *wri*, *bi*, and *f* are the corresponding weight, bias, and activation function for the *rth* neuron, respectively.

Each input MII has two labels. The first one is the one-hot coding for types of modulation format and baud rate for the classification model, and the other is the OSNR value for the regression model. We use four-dimensional vectors to present modulation format and baud rate separately, i.e., [0 0 0 1], [0 0 1 0], [0 1 0 0], and [1 0 0 0]. They represent signals with 12.5 Gbaud PDM-QPSK, 25 Gbaud PDM-QPSK, 12.5 Gbaud PDM-16QAM, and 25 Gbaud PDM-16QAM, respectively. The weights and biases of layers can be updated automatically to minimize the loss function when the model is being trained. For classification NN, the loss function is called cross-entropy (CE)

$$L_{ce} = -\frac{1}{M}\sum_{i=1}^{M}\sum_{c=1}^{N} yi, c \log(\hat{y}i, c) \tag{12}$$

where M and N are the numbers of samples and classes, respectively, and c is the specific class. For the regression model, the loss function is mean squared error (MSE)

$$L_{\text{mse}} = \frac{1}{M}\sum_{i=1}^{M}(y_i - \hat{y}_i)^2 \tag{13}$$

where *yi* is the label, and $\hat{y}i$ represents the output of the neural network. After the training process, the generalization of both neural networks is evaluated by an independent test dataset.

2.3. Polarization splitter-rotator

To deal with the difference of OSNR between in fiber and in silicon waveguide due to polarization issue, we use a polarization splitter-rotator (PSR) to turn the PDM signals into TE mode [42–44],

Optics EXPRESS

as shown in Fig. 3. The upper and lower outputs of PSR can be expressed as

$$\begin{bmatrix} TE_{upper} \\ TE_{lower} \end{bmatrix} = \begin{bmatrix} \alpha & \beta \\ 1-\alpha & 1-\beta \end{bmatrix} \begin{bmatrix} P_X \\ P_Y \end{bmatrix} \tag{14}$$

where P_X and P_Y present the power of x- and y-polarization, respectively. α and β are conversion coefficients from x- and y-polarization to TE mode in the upper path, separately. Based on the fact that the ASE noise is unpolarized [6], OSNR in the upper path can be stated as

$$OSNR_{upper} = \frac{P_{\alpha S_x + \beta S_y}}{P_{0.5N}} \tag{15}$$

where $P_{\alpha S_x + \beta S_y}$ and $P_{0.5N}$ are the optical power of signal and ASE noise in the upper path, separately. Similarly, the OSNR in the lower path is

$$OSNR_{lower} = \frac{P_{(1-\alpha)S_x + (1-\beta)S_y}}{P_{0.5N}} \tag{16}$$

where $P_{(1-\alpha)S_x + (1-\beta)S_y}$ and $P_{0.5N}$ are the optical power of signal and ASE noise in the lower path, separately. The average of the OSNR at the upper and lower path is

$$OSNR = \frac{1}{2}(OSNR_{upper} + OSNR_{\text{lower}}) = \frac{P_{S_x+S_y}}{P_N} \tag{17}$$

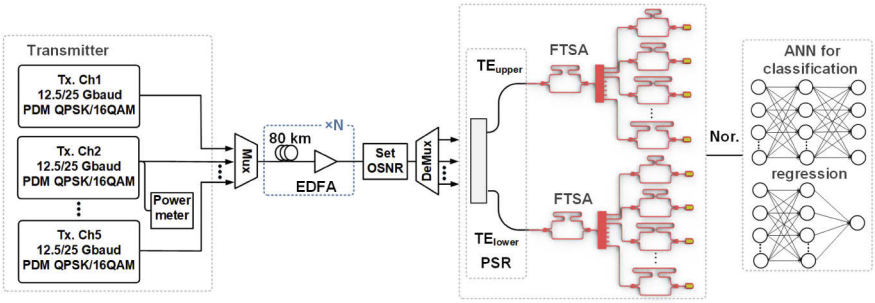

Fig. 3. Simulation setup for OPM (Mux: multiplexer, DeMux: demultiplexer, EDFA: erbium-doped optical fiber amplifier, PSR: polarization splitter-rotator, FTSA: Fourier transform spectrum analyzer, ANN: artificial neural networks)

From Eq. (15–17), we can see that the OSNR at the upper and lower path is different from the true OSNR when the polarizations of fiber and device are mismatched. But the average of the two OSNR values is always identical to the true OSNR. Therefore, we first use FTSA and trained neural networks to determine the OPM parameters of the upper and lower path, respectively. Then the ultimate OSNR is calculated by Eq. (17).

3. Results and discussion

3.1. Simulation setup and neural network training

To demonstrate the feasibility of the proposed scheme, we designed the simulation setup in VPI transmission Maker as shown in Fig. 3. At the transmitter, the polarization division multiplexing (PDM) signals with different modulation formats (QPSK, 16QAM) and baud rates (12.5 Gbaud, 25 Gbaud) were generated. The length of the sequence was $2^{15} - 1$. The linewidth of the laser was

Optics EXPRESS

100 kHz. Channel spacing was set as a 50 GHz ITU grid. The transfer function and the roll-off of the pulse shape filter were raised cosine and 0.18, separately. The power meter was used to measure the launch power of each channel, which was varied from 0 to 6 dBm. The signals with different wavelengths were coupled through the multiplexer, then sent to the fiber link. Each span consisted of a standard single-mode fiber (SSMF) with 80 km and an erbium-doped optical fiber amplifier (EDFA). The attenuation of the SSMF was 0.2 dB/km, and the gain of EDFA was set as 16 dB to fully compensate the fiber attenuation. The number of spans changed from 4 to 20 (320 km to 1600 km) with an interval of 4. There was no ASE noise added in each EDFA and the OSNR was controlled by adding ASE at the end of the fiber link by the Set-OSNR component [32]. The reference OSNR was varied in the range of 5~30 dB with a step of 1 dB. Then, the target channel for OPM was obtained through a demultiplexer, whose bandwidth was channel spacing, i.e., 50 GHz. The configuration parameters of the system are shown in Table 1. For FTSA, the delay of the first-stage MZI was set as 20 ps. The delays of the MZI array at the second stage were set from 15 ps to 25 ps with a 1-ps interval, respectively. The quantity and delay of MZI were determined based on the previous work [45,46] and simulation. Finally, the interference intensities were collected for ANN model training and testing.

Table 1. Key parameters of the system.

Modulation Format		PDM-QPSK and PDM-16QAM
Baud Rate		12.5 Gbaud and 25 Gbaud
Central Frequency		193.1 THz
Laser Linewidth		100 kHz
Quantity of Channels		3 and 5
EDFA Gain		16 dB
SSMF	Attenuation	0.2 dB/km
	Dispersion	16 ps/(nm*km)
	Nonlinear Index	2.6×10^{-20} m^2/W
	Core area	80×10^{-12} m^2
	PMD coefficient	0.032 ps/$(km)^{1/2}$
	Length	80 km
	Span	4-20

Figure 4 shows the transmission functions of FSTA and Demux. In Fig. 4(a), the transmission function of first stage MZI is cosine-shape and the extinction ratio is around 10 dB. Figure 4(b) shows the transmission function of the FTSA with 15-ps, 17-ps, and 19-ps delays in the second stage MZIs, and meanwhile, we keep the delay in the first stage MZI as 20 ps. It can be seen that these transmission functions are also cosine-shape with different free spectral ranges. But all extinction ratios in Fig. 4(b) are more than 20 dB. The higher the extinction ratio, the bigger the difference in interference power between MZIs with different delay values, and the better FTSA can resist environment noise. Superposing a 3-order Gaussian filter, shown in Fig. 4(c), the global transmission function after Demux and FTSA is shown in Fig. 4(d) where the transmission functions are different for different delays. That is, for the same spectrum, the detection intensity of the different ports in FTSA is unequal. As a result, different ports obtain different information of the spectrum.

We employ neural networks to extract the OPM parameter from MIIs for signals with different modulation formats, band rate, OSNR, and transmission conditions. The dataset was randomly divided into a training dataset and a test dataset after MIIs were labeled. The proportions are 85% and 15%, respectively. Two types of neural networks, the classification model (with 12 hidden neurons) and the regression model (with 19 hidden neurons), were trained separately

Optics EXPRESS

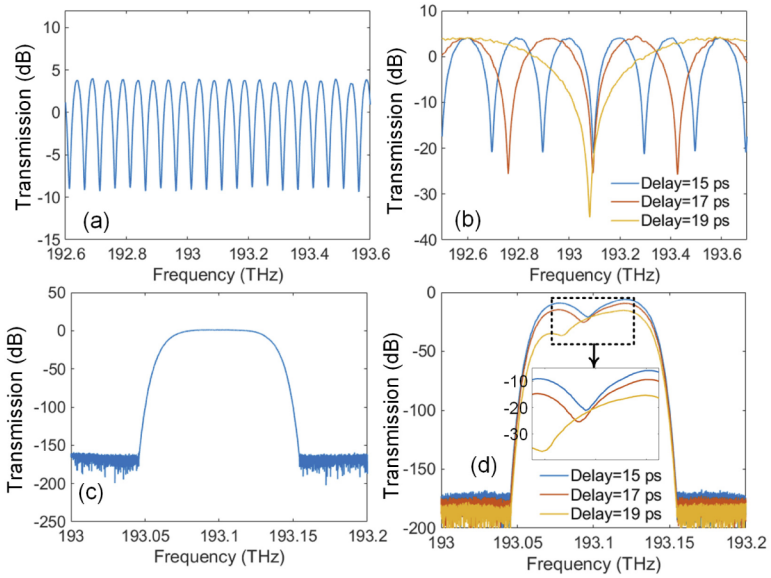

Fig. 4. The transmission function of (a) the first MZI with 20-ps delay, (b) the cascading MZI with different delays (the delay in the first stage was fixed at 20 ps, and the delay in the second stage were set as 15 ps, 17 ps, and 19 ps, respectively) in the second stage, (c) Demux; (d) the global transmission function after Demux and FTSA.

using Bayesian Regularization. The training dataset was supplied into two models, which were then trained and updated using their respective loss functions and optimization algorithms. The criteria for choosing the specific number of neurons in the hidden layer will be illustrated later. The test dataset allowed an objective assessment of the performance of models. The model with low bias and good generalization was achieved when both the training loss and the gap (gap of losses between the training dataset and test dataset) are small enough.

3.2. Modulation format and baud rate recognition

For parts 3.2, 3.3, and 3.4, the whole dataset contains 7280 samples. The variation of the sample parameters is shown in Table 2 where the OSNR changes from 5 to 30 dB with 1-dB interval, the number of the span changes from 4 to 20 with an interval of 4, and so on. Based on the proportion mentioned before, the training dataset has 6188 samples, and the test dataset has 1092 samples, respectively.

Table 2. Variation of sample parameters.

Parameters	Variation range	Quantity
Modulation Format	PDM-QPSK and PDM-16QAM	2
Baud Rate	12.5 Gbaud and 25 Gbaud	2
OSNR	5~30 dB (step of 1dB)	26
Quantity of Channels	3 and 5	2
Launch Power	0–6 dBm (step of 1 dBm)	7
Span	4–20 (step of 4)	5
Total		7280

Optics EXPRESS

Figure 5 shows the confusion matrices of modulation format and baud rate recognition. The numbers 1, 2, 3, and 4, present four kinds of signals (12.5 Gbaud PDM-QPSK, 25 Gbaud PDM-QPSK, 12.5 Gbaud PDM-16QAM, and 25 Gbaud PDM-16QAM). The target class represents the ground truth and the output class is what the neural network predicts. All the correctly classified samples are counted on the diagonal of confusion matrices. It can be noted from the training confusion matrix that the precision rates and recall rates for each class are more than 99.6%and the accuracy of the whole training dataset is 99.8%. We can see a similar pattern from the test confusion matrix. The whole accuracy of the test confusion matrix is 99.6%. It validates that the neural network model possesses a good capability of classification.

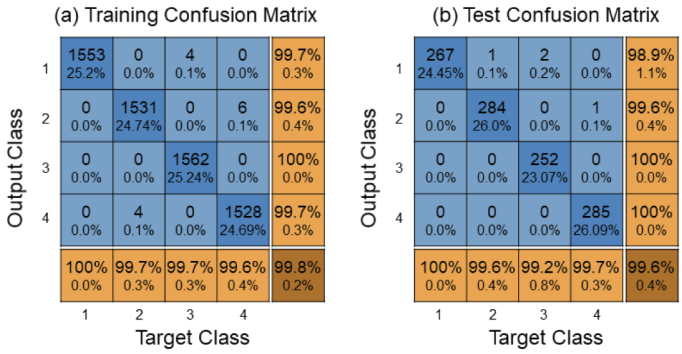

Fig. 5. Confusion matrices of modulation format and baud rate recognition on the (a) training dataset and (b) test dataset.

3.3. OSNR estimation

Figure 6(a) shows the histogram of OSNR monitoring errors on the training dataset and test dataset. It can be seen that most of the OSNR monitoring errors (over 91.06%) are distributed from −0.5 to 0.5 dB. Only a small part of the errors are beyond ±1 dB. The root mean square error (RMSE) of OSNR monitoring is 0.31 dB.

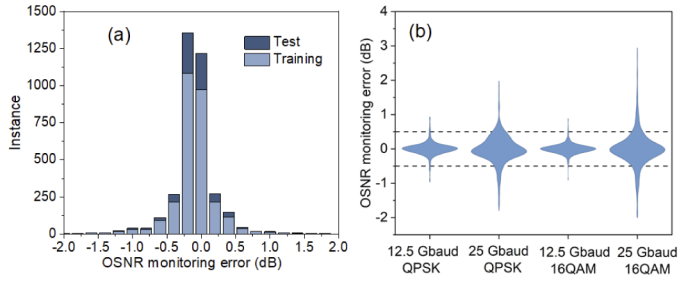

Fig. 6. (a) Histogram of OSNR monitoring errors on the training dataset and test dataset, (b) OSNR monitoring errors on different signal types.

The OSNR monitoring errors for the four types of signals with two modulation formats and two baud rates are shown in Fig. 6(b). The violin-shaped graph denotes the distribution of predicted OSNR errors (1820 samples for each category). It can also be seen that most OSNR monitoring errors are within ±0.5 dB, which is consistent with the results in Fig. 6(a). It should be noted that the monitoring errors are comparatively scattered for 25 Gbaud signals. This is because when OSNR changes, the degree of variation of MII of 25 Gbaud signals is smaller than that of

Optics EXPRESS

12.5 Gbaud signals at a similar channel power level due to the larger bandwidth. And smaller differences between samples are harder to be discriminated by the neural network model.

3.4. Model selection principle of hidden neurons

For ANN, the number of neurons in the hidden layer is a significant parameter because it affects the performance of the model. We varied the number of the hidden neurons from 1 to 30 for both NNs of regression and classification. Each NN with a specific hidden layer was trained and tested 10 times to obtain the error identification rates of the NN for classification and the RMSEs of the NN for regression. To get models with both high accuracy and stability, we defined the comprehensive loss as a new metric.

$$L_{comprehensive} = \mu^2 + \sigma^2 \tag{18}$$

where μ and σ are the mean and standard deviation of results. Therefore, the most stable and accurate model can be selected by finding the lowest comprehensive loss and its corresponding number of neurons. The comprehensive losses for the regression NN and the classification NN are shown in Fig. 7. According to the minimum comprehensive loss, the classification NN with 12 hidden neurons and the regression NN with 19 hidden neurons are chosen.

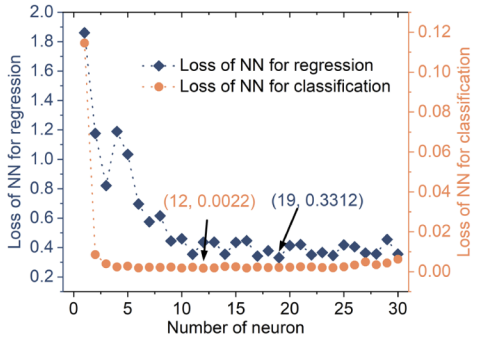

Fig. 7. The comprehensive loss of ANN for regression and classification with a different number of hidden neurons.

3.5. Effect of frequency offset and central frequency

The performance of FTSA will be affected by frequency shift because the transmission function of FTSA is wavelength-dependent. Here we investigate the effects of frequency offsets and central frequency changes. The control variates method was leveraged in this part. First, we altered the central frequency (193.1 THz) of the target channel with a frequency offset from −5 GHz to 5 GHz with an interval of 1 GHz. Meanwhile, the central frequency of other channels and demultiplexer remained unchanged. The dataset with different frequency offsets is shown in Table 3. The NNs are re-trained by the training dataset and the OPM results of the test dataset are shown in Fig. 8(a). Second, we changed the central frequency of the target channel from 193.1 THz to 193.7 THz with an interval of 0.1 THz. The central frequencies of other channels and the demultiplexer changed accordingly. The entire dataset with 25480 samples is shown in Tabel 4.

The results in Fig. 8 show that the accuracies of modulation format and baud rate recognition are all over 99% for different frequency offset and central frequency. Most OSNR monitoring errors (over 91.34%) are less than ±0.5 dB. The results indicate that the retrained NN can cope effectively with changes in frequency offset and center frequency, respectively.

Optics EXPRESS

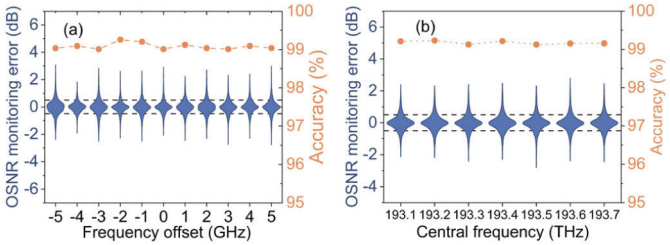

Fig. 8. The accuracy of modulation format and baud rate recognition and the OSNR monitoring error distribution with (a) different frequency offsets and (b) different central frequencies.

Table 3. Variation of sample parameters for investigation of frequency offset.

Parameters	Variation range	Quantity
Modulation Format	PDM-QPSK and PDM-16QAM	2
Baud Rate	12.5 Gbaud and 25 Gbaud	2
OSNR	5~30 dB (step of 1dB)	26
Launch Power	0–6 dBm (step of 1 dBm)	7
Span	4–20 (step of 4)	5
Frequency offset	−5~5 GHz step of 1 GHz)	11
Total		40040

3.6. *Effect of delay jitters*

Delay jitters inevitably exist because of fabrication errors. Generally speaking, fabrication errors within ±50 nm lead to changes of the effective index within ±0.2, giving rise to the delay jitters within ±0.5 ps. To investigate the effect of delays on the performance of FTSA, we introduced delay jitters with a range from −0.5 ps to +0.5 ps randomly to each MZI. Five groups of MZI delays with random jitters, as shown in Table 5, were simulated, and the corresponding dataset is shown in Table 6. The classification and regression models are trained by the dataset containing all of these 5 cases.

Table 4. Variation of sample parameters for investigation of central frequency

Parameters	Variation range	Quantity
Modulation Format	PDM-QPSK and PDM-16QAM	2
Baud Rate	12.5 Gbaud and 25 Gbaud	2
OSNR	5~30 dB (step of 1dB)	26
Launch Power	0–6 dBm (step of 1 dBm)	7
Span	4–20 (step of 4)	5
Central frequency	193.1~193.7 THz (step of 0.1 THz)	7
Total		25480

Figure 9 shows the accuracy of modulation format and baud rate recognition and the OSNR monitoring errors over 5 cases. It can be seen that recognition accuracies and the distribution of OSNR monitoring errors are almost the same from case 1 to case 5. Similar to the behavior observed in the former two sections, the accuracies of modulation format and baud rate recognition are very high (over 99.18%), and most (over 90.93%) OSNR monitoring errors are within ±0.5 dB.

Optics EXPRESS

Table 5. Delays of MZIs in FTSA.

Case	Delays of MZIs in 1st and 2nd stages (ps)
Case 1	**19.57**, 15.36, 15.87, 17.31, 17.88, 18.98, 19.86, 20.94, 22.14, 22.80, 23.09, 25.10
Case 2	**19.54**, 14.79, 15.96, 16.75, 18.30, 18.73, 19.93, 21.45, 21.84, 22.59, 23.72, 25.16
Case 3	**20.03**, 15.11, 15.56, 16.51, 18.32, 18.52, 19.97, 20.72, 21.82, 23.14, 24.39, 25.07
Case 4	**19.89**, 15.06, 15.63, 16.92, 18.31, 18.75, 19.74, 20.53, 21.50, 22.55, 23.96, 24.65
Case 5	**20.42**, 14.96, 15.92, 16.59, 17.93, 19.26, 20.06, 21.04, 22.00, 22.60, 24.02, 25.38

Table 6. Variation of sample parameters for investigation of delay jitter.

Parameters	Variation range	Quantity
Modulation Format	PDM-QPSK and PDM-16QAM	2
Baud Rate	12.5 Gbaud and 25 Gbaud	2
OSNR	5~30 dB (step of 1dB)	26
Launch Power	0–6 dBm (step of 1 dBm)	7
Span	4–20 (step of 4)	5
Delay jitter	Case 1~5	5
Total		18200

These results indicate that the re-trained NN can handle delay jitter between −0.5 and 0.5 ps. In other words, the proposed scheme has high fabrication tolerance for FTSA.

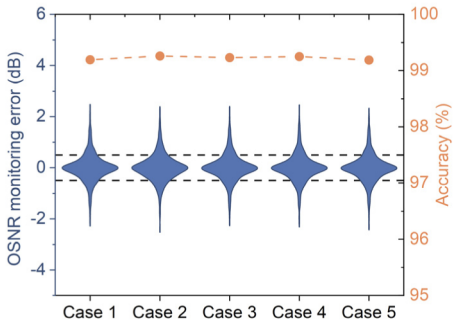

Fig. 9. The accuracies of modulation format and baud rate recognition and the OSNR monitoring error distribution with different delay jitters.

3.7. Combined results

We aggregated all the data in Table 2, 3, 4, 5 and remove the duplicate data of the same situation to generate an overall dataset. The final dataset had 83720 samples, which were divided as 85% training data and 15% test date randomly. The general NNs for classification and regression were trained separately using the training data. Different central frequencies, frequency offsets, and delay jitters of FTSA were compatible with these general NNs. The results of the test data are shown in Fig. 10 where the accuracy of modulation format and baud rate recognition is 94.8%, and most OSNR monitoring errors are less than ±1 dB. It is undeniable that the OPM performance has deteriorated as compared to prior parts. However, the performance of OPM is acceptable, with improved robustness and versatility. This is due to the fact that the dataset is considerably larger than before, and the generalization develops with the sacrifice of high accuracies results from overfitting. To intuitively show the probability of OSNR monitoring errors distribution, we

Optics EXPRESS

calculated the absolute error and exhibit the complementary cumulative distribution function (CDF) in Fig. 10(c). The value of the point in this curve represents the probability that events happen when the error is larger than the abscissa of this point. For example, the value of the curve at 0 dB error is 1 indicates that all absolute errors are larger than zero; the value of 1-dB error is 0.14, which indicated that 14% of predictions have absolute errors larger than 1 dB. In other words, 86% of OSNR monitoring absolute errors are within 1 dB.

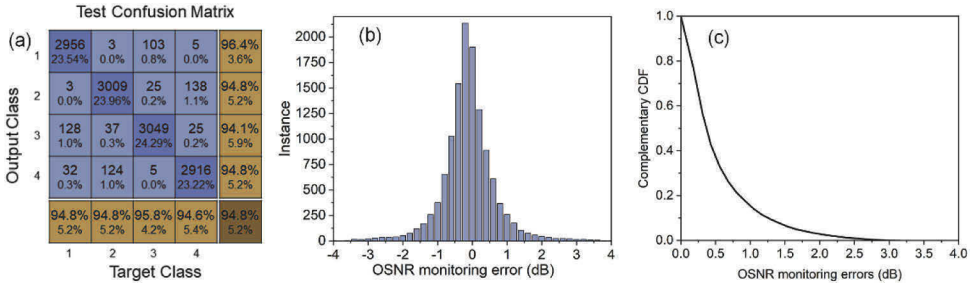

Fig. 10. (a) The accuracy of modulation format and baud rate recognition and (b) the histogram of OSNR monitoring errors on test data for general neural networks; (c) the complementary cumulative probability distribution function of OSNR monitoring errors.

Furthermore, the OSNR and frequency offset in the system varied randomly after the optical performance monitor was installed, therefore we investigated the performance of the neural networks for the unpredictable OSNRs and frequency offsets. First, the 25 OSNR values of 5.79, 6.15, 7.42, 8.12, 9.27,10.36, 11.92, 12.92, 13.21, 14.53, 15.96, 16.77, 17.24, 18.93, 19.22, 20.56, 21.15, 22.37, 23.57, 24.13, 25.58, 26.70, 27.25, 28.75, 29.33 with uniform distribution from 5 to 30 dB were under test. Then, we altered the frequency offset from −5 to 5 GHz at random (−4.47 GHz, −3.69 GHz, 1.18 GHz, 2.62 GHz, and 4.88 GHz). Finally, we generated 35000 samples to test the trained neural network as indicated in Table 7, and the results are displayed in Fig. 11. It can be seen that the similar performance for modulation format and baud rate recognition, and OSNR monitoring is obtained, indicating that the trained neural network is to some extent compatible with random OSNRs and random frequency offsets in the system, although the neural network was not trained with the exact same samples of random OSNRs and frequency offsets.

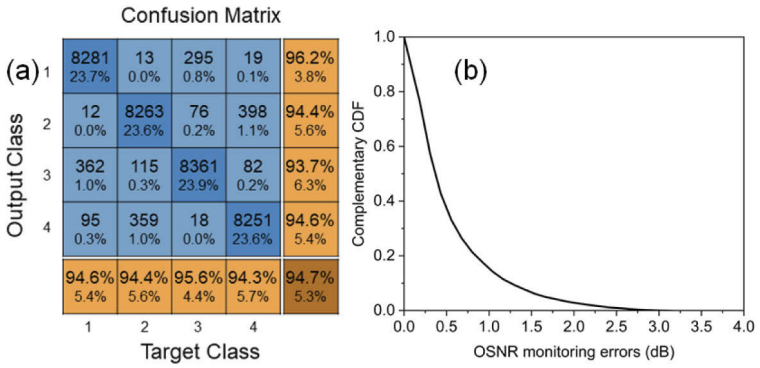

Fig. 11. (a) The accuracy of modulation format and baud rate recognition and (b) the complementary cumulative probability distribution function of OSNR monitoring errors for random OSNR and random frequency offsets.

Optics EXPRESS

Table 7. Variation of sample parameters for random OSNR and frequency offset.

Parameters	Variation range	Quantity
Modulation Format	PDM-QPSK and PDM-16QAM	2
Baud Rate	12.5 Gbaud and 25 Gbaud	2
Quantity of Channels	3 and 5	2
Launch Power	0–6 dBm (step of 1 dBm)	7
Span	4–20 (step of 4)	5
OSNR	25 random values	25
Frequency offset	5 random values	5
Total		35000

4. Conclusion

In this paper, we proposed a multi-parameter optical performance monitoring method based on Fourier transform spectral analysis and artificial neural networks. For 12.5/25 Gbaud PDM-QPSK/16QAM signals under complex transmission conditions, the accuracy of the modulation format and baud rate recognition is 94.8% and the OSNR monitoring errors are mostly (over 86%) within ±1 dB with a range from 5 to 30 dB in presence of nonlinearity. As the quality of transmission components such as laser, device manufacturing improves, the accuracy of identification will be increased to 99.6% and OSNR monitoring errors will be less than 0.5 dB. The Fourier transform spectrum analyzer has large fabrication tolerance and broad bandwidth to support WDM communication systems. On the other hand, the CD, PMD, and PDL have little impact on the shape of the spectrum, and thus have little impact on OPM performance.The method is integrable and cost-effective, indicating that it can be applied in the numerous intermediate nodes of optical networks. We will carry out the fabrication and test in the future. Besides, this method is general, which can be applied universally to short-reach, long-haul, CWDM, or DWDM links with or without nonlinearity.

Funding. National Natural Science Foundation of China (62005030); Chongqing Innovative Research Groups (No. CXQT20001); Research Grants Council, University Grants Committee (15211619).

Disclosures. The authors declare no conflicts of interest.

Data availability. Data underlying the results presented in this paper are not publicly available at this time but may be obtained from the authors upon reasonable request.

References

1. I. Yaqoob, I. A. T. Hashem, Y. Mehmood, A. Gani, S. Mokhtar, and S. Guizani, "Enabling communication technologies for smart cities," IEEE Commun. Mag. **55**(1), 112–120 (2017).
2. M. Jaber, M. A. Imran, R. Tafazolli, and A. Tukmanov, "5G backhaul challenges and emerging research directions: A survey," IEEE Access **4**, 1743–1766 (2016).
3. Z. Dong, F. N. Khan, Q. Sui, K. Zhong, C. Lu, and A. P. T. Lau, "Optical performance monitoring: A review of current and future technologies," J. Lightwave Technol. **34**(2), 525–543 (2016).
4. I. Roberts and J. M. Kahn, "Efficient discrete rate assignment and power optimization in optical communication systems following the Gaussian noise model," IEEE J. Lightw. Technol. **35**(20), 4425–4437 (2017).
5. A. D. Shiner, M. E Mousa-Pasandi, M. Qiu, M. A. Reimer, E. Y. Park, M. Hubbard, Q. Zhuge, F. J. V. Caballero, and M. O'Sullivan, "Neural network training for OSNR estimation from prototype to product," in *Proc. Optical Fiber Communication Conference* (OSA, 2020), pp. M4E.2.
6. J. H. Lee, H. Y. Choi, S. K. Shin, and Y. C. Chung, "A review of the polarization-nulling technique for monitoring optical-signal-to-noise ratio in dynamic WDM networks," J. Lightwave Technol. **24**(11), 4162–4171 (2006).
7. L. Lundberg, H. Sunnerud, and P. Johannisson, "In-band OSNR monitoring of PM-QPSK using the Stokes parameters," in *Proc. Optical Fiber Communication Conference* (OFC, 2015), pp. W4D. 5.
8. Z. Huang, J. Qiu, D. Kong, Y. Tian, Y. Li, H. Guo, X. Hong, and J. Wu, "A novel in-band OSNR measurement method based on normalized autocorrelation function," IEEE Photon. Journal **10**(2), 1–8 (2018).

Optics EXPRESS

9. F. Locatelli, K. Christodoulopoulos, M. S. Moreolo, J. M. Fàbrega, and S. Spadaro, "Machine learning-based in-band OSNR estimation from optical spectra," IEEE Photonics Technol. Lett. **31**(24), 1929–1932 (2019).
10. V. López and L. Velasco, *Elastic Optical Networks, Architectures, Technologies, and Control* (Springer Int. Publishing, 2016).
11. Y. Li, Q. Zheng, J. Han, and W. Li, "Low complexity carrier phase estimation for m-QAM optical communication systems," Photon. Netw. Commun. **38**(1), 121–128 (2019).
12. Z. Zhu and A. K. Nandi, Automatic Modulation Classification: Principles, *Algorithms and Applications* (Wiley, 2015).
13. A. Amari, X. Lin, O. A. Dobre, R. Venkatesan, and A. Alvarado, "A machine learning-based detection technique for optical fiber nonlinearity mitigation," IEEE Photonics Technol. Lett. **31**(8), 627–630 (2019).
14. A. G. Reza and J. K. Rhee, "Nonlinear equalizer based on neural networks for PAM-4 signal transmission using DML," IEEE Photonics Technol. Lett. **30**(15), 1416–1419 (2018).
15. Z. Wan, J. Li, L. Shu, M. Luo, X. Li, S. Fu, and K. Xu, "Nonlinear equalization based on pruned artificial neural networks for 112-Gb/s SSB-PAM4 transmission over 80-km SSMF," Opt. Express **26**(8), 10631–10642 (2018).
16. E. Giacoumidis, A. Matin, J. Wei, N. J. Doran, L. P. Barry, and X. Wang, "Blind nonlinearity equalization by machinelearning-based clustering for single- and multichannel coherent optical OFDM," J. Lightwave Technol. **36**(3), 721–727 (2018).
17. C. Häger and H. D. Pfister, "Deep learning of the nonlinear Schrödinger equation in fiber-optic communications," in *Proc. IEEE Int. Symp. Inf. Theory (ISIT)*, 1590–1594 (2018).
18. J. Du, T. Yang, X. Chen, J. Chai, Y. Zhao, and S. Shi, "A CNN-based cost-effective modulation format identification scheme by low-bandwidth direct detecting and low rate sampling for elastic optical networks," Optics Comm., **471**, (2020).
19. D. Wang, M. Wang, M. Zhang, Z. Zhang, H. Yang, J. Li, J. Li, and X. Chen, "Cost-effective and data size–adaptive OPM at intermediated node using convolutional neural network-based image processor," Opt. Express **27**(7), 9403–9419 (2019).
20. Y. Cheng, S. Fu, M. Tang, and D. Liu, "Multi-task deep neural network (MT-DNN) enabled optical performance monitoring from directly detected PDM-QAM signals," Opt. Express **27**(13), 19062–19074 (2019).
21. F. N. Khan, Y. Yu, M. C. Tan, W. H. Al-Arashi, C. Yu, A. P. T. Lau, and C. Lu, "Experimental demonstration of joint OSNR monitoring and modulation format identification using asynchronous single channel sampling," Opt. Express **23**(23), 30337–30346 (2015).
22. X. Fan, Y. Xie, F. Ren, Y. Zhang, X. Huang, W. Chen, T. Zhangsun, and J. Wang, "Joint Optical Performance Monitoring and Modulation Format/Bit-Rate Identification by CNN-Based Multi-Task Learning," IEEE Photonics J. **10**(5), 1–12 (2018).
23. J. Thrane, J. Wass, M. Piels, J. C. M. Diniz, R. Jones, and D. Zibar, "Machine learning techniques for optical performance monitoring from directly detected PDM-QAM signals," J. Lightwave Technol. **35**(4), 868–875 (2017).
24. D. Wang, M. Zhang, J. Li, Z. Li, J. Li, C. Song, and X. Chen, "Intelligent constellation diagram analyzer using convolutional neural network-based deep learning," Opt. Express **25**(15), 17150–17166 (2017).
25. Q. Zhang, Y. Yang, C. Guo, X. Zhou, Y. Yao, A. P. T. Lau, and C. Lu, "Accurate BER Estimation Scheme Based on K-Means Clustering Assisted Gaussian Approach for Arbitrary Modulation Format," J. Lightwave Technol. **38**(8), 2152–2157 (2020).
26. L. Guesmi, A. M. Ragheb, H. Fathallah, and M. Menif, "Experimental Demonstration of Simultaneous Modulation Format/Symbol Rate Identification and Optical Performance Monitoring for Coherent Optical Systems," J. of Lightw. Technol. **36**(11), 2230–2239 (2018).
27. F. J. V. Caballero, D. J. Ives, C. Laperle, D. Charlton, Q. Zhuge, M. O'Sullivan, and S. J. Savory, "Machine Learning Based Linear and Nonlinear Noise Estimation," J. Opt. Commun. Netw. **10**(10), D42–51 (2018).
28. H. Zheng, W. Li, M. Mei, Y. Wang, Z. Feng, Y. Chen, and W. Shao, "Modulation format-independent optical performance monitoring technique insensitive to chromatic dispersion and polarization mode dispersion using a multi-task artificial neural network," Opt. Express **28**(22), 32331–32341 (2020).
29. C. Hu, H. Zheng, W. Li, Q. Feng, M. Mei, Y. Wang, and R. Yan, "Modulation-format-independent in-band OSNR monitoring technique using Gaussian process regression for a Raman amplified multi-span system with a cascaded filtering effect," Opt. Express **28**(7), 10134–10144 (2020).
30. F. N. Khan, K. Zhong, X. Zhou, W. H. Al-Arashi, C. Yu, C. Lu, and A. P. T. Lau, "Joint OSNR monitoring and modulation format identification in digital coherent receivers using deep neural networks," Opt. Express **25**(15), 17767–17776 (2017).
31. F. N. Khan, K. Zhong, W. H. Al-Arashi, C. Yu, C. Lu, and A. P. T. Lau, "Modulation Format Identification in Coherent Receivers Using Deep Machine Learning," IEEE Photonics Technol. Lett. **28**(17), 1886–1889 (2016).
32. Z. Wang, A. Yang, P. Guo, and P. He, "OSNR and nonlinear noise power estimation for optical fiber communication systems using LSTM based deep learning technique," Opt. Express **26**(16), 21346–21357 (2018).
33. M. C. Tan, F. N. Khan, W. H. Al-Arashi, Y. Zhou, and A. P. T. Lau, "Simultaneous optical performance monitoring and modulation format/bit-rate identification using principal component analysis," J. Opt. Commun. Netw. **6**(5), 441–448 (2014).
34. C. Hu, W. Li, H. Zheng, Q. Feng, Q. Zheng, and Y. Wang, "A novel cost-effective and distributed in-band OSNR monitoring method using Gaussian process regression," IEEE Photonics J. **11**(4), 1–12 (2019).

Optics EXPRESS

35. P. Zhang, L. Xi, J. Yuan, X. Tang, W. Zhang, J. Li, and X. Zhang, "Fiber nonlinearity-insensitive OSNR monitoring for coherent PM-QPSK-Nyquist-WDM system," Optical Fiber Technol. **36**, 215–221 (2017).
36. M. Nakajima, K. Suzuki, K. Seno, R. Kasahara, T. Goh, Y. Miyamoto, and T. Hashimoto, "Optical Arbitrary Waveform Processing of Over 100 Spatial Channels for Optical Performance Monitoring," J. of Lightw. Technol. **37**(2), 291–299 (2019).
37. K. Tanizawa, K. Sorimoto, K. Suzuki, K. Ikeda, S. Namiki, and H. Kawashima, "In-band OSNR monitor based on 3 × 3 Si-wire MMI coupler," in *European Conference on Optical Communication* (OFC 2015), pp. 0270.
38. J. Qiu, Y. Tian, Z. Huang, Y. Wang, D. Kong, and J. Wu, "Integrablerated In-Band OSNR Monitor Based on Asymmetrical Parallel-MZIs for WDM signals," IEEE J. Select. Topics Quantum Electron. **22**(6), 467–472 (2016).
39. M. Florjanczyk, P. Cheben, S. Janz, A. Scott, B. Solheim, and D. Xu, "Multiaperture planar waveguide spectrometer formed by arrayed Mach-Zehnder interferometers," Opt. Express **15**(26), 18176–18189 (2007).
40. S. N. Zheng, J. Zou, H. Cai, J. F. Song, L. K. Chin, P. Y. Liu, Z. P. Lin, D. L. Kwong, and A. Q. Liu, "Microring resonator-assisted Fourier transform spectrometer with enhanced resolution and large bandwidth in single chip solution," Nat. Commun. **10**(1), 1–8 (2019).
41. A. D. Dongare, R. R. Kharde, and A. D. Kachare, "Introduction to artificial neural network," International Journal of Engineering and Innovative Technology **2**(1), 189–194 (2012).
42. W. D. Sacher, T. Barwicz, B. J. F. Taylor, and J. K. S. Poon, "Polarization rotator-splitters in standard active silicon photonics platforms," Opt. Express **22**(4), 3777–3786 (2014).
43. A. H. K. Park, H. Shoman, M. Ma, S. Shekhar, and L. Chrostowski, "Ring resonator based polarization diversity WDM receiver," Opt. Express **27**(5), 6147–6157 (2019).
44. Z. Lin, T. Dadalyan, S. B. Villers, T. Galstian, and W. Shi, "Chip-scale full-Stokes spectropolarimeter in silicon photonic circuits," Photon. Res. **8**(6), 864–874 (2020).
45. Z. Huang, Y. Tian, X. Long, C. Zhang, and Y. Liu, "Fourier Transform Spectral Analysis Based Fiber Nonlinearity-insensitive OSNR Monitor," *Conference on Lasers and Electro-Optics* (CLEO 2021), pp. JW1A.117.
46. H. Luo, Z. Huang, and C. Yu, "Optimization on integrated Fourier transform spectrum analyzer for optical performance monitoring," *26th Optoelectronics and Communications Conference* (OECC2021), pp. T1B.2.